Enhancing the electrical conductivity of *in-situ* reduced graphene oxide-zirconia composites through the control of the processing routine

Cristina López-Pernía[*] [a,b], Ana Morales-Rodríguez [a], Ángela Gallardo-López [a], Rosalía Poyato [b]

a. Depto. de Física de la Materia Condensada. ICMS, CSIC-Universidad de Sevilla. Apdo. 1065. 41080 Sevilla. Spain

b. Inst. Ciencia de Materiales de Sevilla, ICMS, CSIC-Universidad de Sevilla. Américo Vespucio 49. 41092 Sevilla. Spain

Abstract

Graphene oxide (GO) was mixed with 3 mol% yttria tetragonal zirconia polycrystal (3YTZP) using two powder processing routines: a colloidal method in an aqueous solution and a combination of ultrasonication with high-energy planetary ball milling in wet conditions. Highly densified 3YTZP composites with reduced GO (rGO) were consolidated by Spark Plasma Sintering. The *in-situ* reduction of GO was successfully achieved during the high-temperature sintering process and a detailed study of the

[*] Corresponding autor. E-mail: cristinalopez@us.es (Cristina López-Pernía)

restoration of the graphene structure in the sintered composites has been made by Raman spectroscopy. Although no differences between the composites prepared by the two processing methods were found in the distribution of the rGO throughout the 3YTZP matrix for high rGO contents (i.e. the composites with 5 and 10 vol% rGO), a better distribution of the graphene phase was found in the composites with 1 and 2.5 vol% rGO prepared by planetary ball milling. This result, together with a better reduction of the GO in these composites, led to the obtaining of rGO/3YTZP composites with a better behavior in terms of electrical conductivity: an electrical percolation threshold below 2.5 vol% rGO and a high electrical conductivity value (~ 610 S/m for 10 vol% rGO).

Keywords: reduced graphene oxide, composites, sintering, electrical conductivity

1. Introduction

Since 2004, graphene has become a fascinating material in several areas of science and technology. It presents extraordinary unprecedented properties that make it an advantageous material to be employed in many different applications. Among them, stands out its use in the fabrication of composite materials, as it has been considered as a potential reinforcement filler in metallic, polymeric and ceramic matrices [1,2]. The typical approach to produce high-quality "pristine" graphene (a monolayer of carbon atoms free of defects) consists on the mechanical cleavage of bulk graphite [3]. However, this technique does not provide large enough quantities of graphene to be used as a composite filler [4]. Thus, other carbon nanostructures, such as few-layer graphene or graphene oxide (GO) have emerged as easier to obtain alternatives with similar functionalities [5]. In this sense, the production of advanced ceramic composites with graphene-based nanomaterials (GBNs) has become an interesting topic for the scientific community.

In the last decade, several researchers have reported the enhancement of the mechanical, thermal and electrical properties of ceramics such as Si_3N_4 [6–8], SiC [9], Al_2O_3 [10–12] or ZrO_2 [13,14] when adding GBNs like GO. Conversely to graphene, GO is electrically insulating due to its sp^2 network disrupted with several functional groups [15]. However, when GO is reduced, the graphene network is restored and the material becomes electrically conductive. Therefore, reduced graphene oxide (rGO) can be used to produce electro-conductive ceramic composites. The reduction of GO is an essential step in the development of these materials and is commonly carried out by applying chemical or thermal treatments before sintering [6,10,14]. Recently, some researchers have reported the possibility of skipping this additional step of the process and taking

advantage of the conditions of the Spark Plasma Sintering (SPS) technique (vacuum atmosphere and high temperatures) to *in-situ* reduce the GO during the sintering of the ceramic composites [7,12,16,17]. Although Raman spectroscopy has been shown to be an effective technique to characterize the degree of reduction of graphene oxide [18], to the best of our knowledge, a comprehensive Raman analysis of the reduction of the GO sheets after the consolidation of GO-ceramic composites through SPS has not been reported so far. Thus, considering that the degree of reduction of GO is a key factor for the enhancement of the electrical response of these composites, it is interesting and necessary to make a deeper analysis of the Raman spectra of the GO sheets present in these materials.

The effect of the addition of reduced graphene oxide (rGO) on the microstructure and properties of ceramic composites has been treated in depth in alumina, silicon carbide and silicon nitride composites [6–12], but the studies about zirconia composites are not so common. Zirconia-based ceramics are very attractive structural materials because of their outstanding mechanical properties and corrosion resistance. Among them, 3 mol% yttria tetragonal zirconia polycrystals (3YTZP) stands out for its high fracture toughness attributed to the tetragonal to monoclinic transformation, which impedes fracture propagation [19]. In 2014, Shin et al. [14] first reported that the fracture toughness of zirconia/rGO composites increased up to 5.9 $MPa^{1/2}$ and an electrical conductivity of $1.2x10^4$ S/m was obtained when 4.1 vol% of rGO was added to the ceramic matrix. Solis et al. [13] also reported that a content of 2.75 vol% rGO would be enough to produce composites with electrical resistivity < 100 Ω cm, so they could be machined by using electro-discharge machining (EDM) techniques while maintaining the mechanical properties of zirconia. A critical step to obtain these composites with superior properties is the mixing of the GO and the ceramic powder, since

homogeneous dispersions of rGO in the ceramic matrix after sintering are needed to improve the behavior of the final materials. Most of the work reported on the preparation of GO-zirconia composite powders is related to processing routes that involve ultrasonication in dispersants, such as DMF [14], and colloidal routes in aqueous solutions [13,16]. Regarding other ceramic systems, Wang et al. [10] and Centeno et al. [12] prepared rGO-alumina ceramic composites via the colloidal route from suspensions of GO and alumina in water at a pH of 11 and 10, respectively. Walker et al. [6] also employed the colloidal processing method to successfully produce graphene-Si_3N_4 composites. Other more energetic powder processing techniques, like ball milling, have also been used to prepare graphene-ceramic composites with homogeneous microstructures. These techniques are most likely used with other GBN, like graphene nanoplatelets (GNP), due to their potential resistance to structural damage [20,21]. However, Hanzel et al. [9] reported that the use of ball milling during 24 h produces SiC composites with a better behavior in terms of electrical conductivity when rGO was used instead of GNP. They explained that the higher interplanar distance between the GO layers favors its delamination during the milling process [9]. In this sense, Bonieki et al. [22] employed planetary ball milling during a short time of 15 min to produce GO-alumina/zirconia composites and Chen et al. [23] used this method for 24 h after the ultrasonication of GO/ZrO_2 powders. In rGO/zirconia composites, more complete works about electrical properties have been carried out in composites from powders obtained by colloidal methods [13,14], while the works in which ball milling was used focus mainly in the mechanical properties of the sintered composites [22,23]. Therefore, it becomes really motivating to further analyze the effect of these two different processing routes –colloidal processing and ball milling– on the electrical conductivity of the rGO/zirconia composites.

This work aims to compare two powder processing routines –a colloidal technique and a method involving planetary ball milling– to prepare composites of 3YTZP with content ranging from 1 to 10 vol% of reduced graphene oxide (rGO), in order to establish the most adequate one in terms of the electrical conductivity of the composites. With the purpose of attaining the *in-situ* reduction of GO, the composites have been consolidated by Spark Plasma Sintering. The restoration of the graphene structure after the sintering thermal treatment has been thoroughly analyzed by Raman spectroscopy and the differences between the composites prepared by the two different routines have been established. The effect of the rGO content on the mechanical and electrical properties of the sintered composites has been analyzed and related to the microstructural features of the composites.

2. Experimental

2.1. Composite powder processing and sintering

Two different procedures have been carried out to mix the 3YTZP powder (40 nm particle size, Tosoh Corporation, Tokyo, Japan) with a commercial GO powder, with a thickness of 2-3 nm and lateral dimension of approximately 7 μm (N002-PDE, Angstron Materials, Dayton, Ohio, USA). The as-received 3YTZP powder was annealed at 850 ºC for 30 min in air before preparing the composite powders.

In the colloidal routine, the 3YTZP powder was dispersed under continuous magnetic stirring in distilled water with a few drops of NH_4OH (to fix the pH value to 10). Also, a dispersion of GO was similarly prepared and added gradually to the 3YTZP suspension. Then, the colloidal suspension was dried on a hot plate while maintaining magnetic stirring and keeping the pH value at 10 during water evaporation. Finally, the composite powders were ground in an agate mortar.

In the ball milling routine, the GO powder was dispersed in ethanol using ultrasonic agitation for 15 minutes in time intervals of 5 min to avoid extreme heating of the suspension. Then, the 3YTZP powder was added to the GO suspension and the mixture was subjected to ultrasonication for 5 more minutes. A KT-600 ultrasonic probe (Kontes, Inc., Vineland, NJ) operating at 20 kHz and 95% amplitude was used to perform the agitation treatments. Finally, the suspension was milled in a planetary ball-mill (Pulverisette 7, Fritsch, Germany) in wet conditions. Seven zirconia balls with a diameter of 15 mm were used as the milling media. The suspension was introduced with the balls in a 45 ml zirconia jar. A slow speed (250 rpm) and short milling time (15 min) were chosen to avoid the damage to the GO layers. Finally, the powders were dried in a rotary evaporator and homogenized in an agate mortar.

For both processes, composite powders with 1, 2.5, 5 and 10 vol% GO were prepared. The prepared powders are named as xGO_C, for the ones prepared by the colloidal method and xGO_PBM, for the ones prepared using ultrasonication followed by planetary ball milling. The x refers to the nominal GO vol% in the composite powders.

Disc samples of 15 mm diameter were consolidated by SPS (Model 515S, SPS Dr Sinter Inc. Kanagawa Japan, Centro de Investigación, Tecnología e Innovación de la Universidad de Sevilla, CITIUS) at 1250 ºC for 5 min with an applied uniaxial pressure of 75 MPa. The temperature was controlled during the heating process using a pyrometer, which was focused on the surface of the graphite die. For each pellet, ~3 g of composite powder was introduced into a graphite die. The sintering process was carried out in vacuum, so the reduction of GO was expected to occur *in-situ* during the sintering process. A similar nomenclature to the one used to name the different powders is proposed for the sintered composites by adding the letter “r” to account for reduced

GO: xrGO_C refers to the sintered composites prepared through the colloidal method, and xrGO_PBM refers to the ones prepared by the combination of ultrasonic agitation and planetary ball milling.

2.2. Characterization of the composite powders and sintered specimens

2.2.1 Density

The Archimedes' method was used to determine the density of the composites. Distilled water was used as the immersion medium. Density values of 6.05 g/cm^3 and 2.20 g/cm^3 for the 3YTZP and GO, respectively, were used to calculate the theoretical density of the composites by the rule of mixtures.

2.2.2 Microstructural characterization

The semi-quantitative analysis of the crystallographic phases present in the sintered composites was carried out by X-Ray diffraction (XRD) at CITIUS in a D8 Advanced A25 X-Ray diffractometer (Bruker Co. Massachussetts, USA).

The *in-situ* reduction of GO during the sintering process was assessed by Raman spectroscopy, by comparing the spectra acquired on the as-received GO as well as on the as-processed composite powders and on the sintered composites. At least ten spectra were acquired in different regions of each specimen using a LabRam HR800 spectrometer (Horiba Jobin Yvon, Kyoto, Japan) operating at 532.14 nm (Instituto de Ciencia de Materiales de Sevilla, ICMS). Raman measurements were recorded in the as-received GO powders, the composite powders and the fracture surfaces of the sintered composites. The Raman spectra were fitted to a combination of functions [24,25] using the Origin 8.5 software. In order to perform the fitting of the first-order Raman spectra (1000-2000 cm^{-1}), Gaussian functions were used to fit D* and D'' bands, whereas D, G

and D' bands were fitted using pseudo-Voigt functions. These functions were used for both the composite powders and the sintered composites spectra fits. In the second-order Raman spectra (2000-3500 cm^{-1}) of the powders, pseudo-Voigt functions were used to fit the G*, 2D, D+D' and 2D' bands. In the sintered composites, the best fit of the 2D band was achieved by using three Lorentz functions, whereas the G*, D+D' and 2D' were also fitted by pseudo-Voigt functions.

Scanning electron microscopy (SEM) was used to observe the distribution of the rGO in the ceramic matrix and the morphology of the 3YTZP ceramic grains. In order to evaluate the degree of anisotropy of the composites, a conventional SEM (FEI-Teneo, CITIUS) was used to observe the composite cross-section (c.s.) and top-view (t.v.) surfaces, previously polished with diamond paste up to 1 µm. Back scattered electrons (BSE) imaging was used for imaging the distribution and homogeneity of the rGO throughout the ceramic matrix. To characterize the ceramic grains, polished c.s. surfaces were thermally revealed at 1150 ºC for 15 min in air. The equivalent planar diameter $d = 2(area/\pi)^{1/2}$ was used to estimate the 3YTZP grain size. The shape factor of the grains was calculated as $F = 4\pi\ area/(perimeter)^2$. The ImageJ and Origin 8.5 softwares were used to quantify these morphological parameters, analyzing more than 500 grains for each composite. The grain size distribution for each specimen was fitted to a log-normal distribution to quantify the mean grain size values.

2.2.3 Elastic modulus and Vickers hardness

The Young's modulus of the composites was measured at room temperature using the impulse excitation technique. Sonelastic® equipment and software (ATCP Physical Engineering, Riberao Preto, Brazil) have been used to measure the acoustic response of disc-shaped samples to a short mechanical pulse.

The hardness of the composites was estimated on in-plane and cross sections from Vickers indentations. At least 10 indentations were performed on the corresponding polished surface of the composites with a Vickers Duramin micro-indenter (Struers) and a normal load of 1.96 N. The hardness values were calculated using the equation $H_V(GPa) = 1854.4\ P/D^2$, where D is the average diagonal of the imprint (in μm) and P the applied load (in N).

2.2.4 Electrical properties

The DC electrical conductivity of the sintered composites was measured at room temperature with a Solartron SI 1260A (Ametek Scientific Instruments, Berwyn, PA, USA, CITIUS) using a potentiodynamic method with a 0-10 mV range in steps of 1 mV. In order to evaluate the degree of electrical anisotropy of the composites, two different electrode configurations were used to measure the conductivity in the directions parallel ($\sigma_{\parallel}$) and perpendicular ($\sigma_{\perp}$) to the SPS pressing axis. Silver electrodes were prepared by coating with colloidal silver painting the corresponding two parallel surfaces of each sample, the cross-sections for measuring $\sigma_{\perp}$, and the in-planes for $\sigma_{\parallel}$. Then, the electrodes were annealed at 600 ºC for 30 min in argon flow.

3. Results and discussion

3.1. Density and microstructure

Nearly fully dense composites, with relative densities ≥ 98%, were obtained after sintering by SPS (Table 1).

In order to verify the prevalence of the tetragonal phase after the sintering process, a semi-quantitative XRD analysis of the composites was carried out. Figure 1 shows the XRD patterns of the sintered composites, which indicate the reduced tetragonal zirconia

($ZrO_{1.95}$) (JCPDS 081-1544) as the main phase in all the composites. The presence of a reduced state of the tetragonal phase is consequence of the sintering under reduction conditions and has been reported in previous works [26–28]. However, in the composites with 10 vol% rGO content prepared through the colloidal method, a small content of monoclinic phase (JCPDS 037-1484) is noticed (see inset in figure 1a).

Figure 2a and 2b shows the Raman spectra from the as-received GO powder and the composite powders prepared by both processing routines. As it can be observed in this figure, the spectra from the composite powders are analogous to the one of the as-received GO powders. In these spectra, the characteristic D and G bands of GO located at ~1350 and ~ 1585 cm^{-1}, respectively, and a group of bumps centered at ~ 2900 cm^{-1} have been detected. In addition to the bands that can be clearly observed, other features related to defects are present in the spectra. In the first-order region (1000-2000 cm^{-1}), a peak overlapped with the left side of the D band is observed below 1200 cm^{-1} and a broad shoulder appears between the D and G peaks (~1500 cm^{-1}). These features correspond, respectively, to the D* and D" bands present in defective graphite-related materials [24]. Moreover, the observed G peak has been reported to be an apparent G band (G_{app}) formed by the sum of the intensities of the real G peak and a defect-related peak known as D' [24]. The bumps observed in the second-order region (2250-3500 cm^{-1}) correspond to up to four different bands (G*, 2D, D+D' and 2D'), that are also characteristic of graphitic materials [29,30].

The D peak is typically considered as the band of disorder in graphitic materials, so usually high values of I_D/I_G are related to the presence of defects on the graphene lattice. The I_D/I_G ratio has been commonly reported by means of the intensities (heights) of the D and the apparent G bands and it is not considered that the contribution of the D*, D''

and D’ peaks can distort the real intensities [31]. Therefore, some of the I_D/I_G values reported in literature are not reflecting the true intensity ratio. Moreover, the D*, D” and D’ bands can also provide information about the structural organization of GO [24,32]. Therefore, in order to properly analyze the Raman spectra of the composite powders, the spectra were normalized respect to the G_{app} band and the D*, D, D”, G and D’ peaks were fitted to three pseudo-Voigt (D, G and D’ bands) and two Gaussian (D* and D” bands) functions so their positions (x_i), widths (w_i) and integrated areas (A_i) were obtained. In the same way, the bumps at ~ 2900 cm^{-1} in the second-order Raman spectra (2250-3500 cm^{-1}) of the powders were fitted to four pseudo-Voigt functions to obtain also the peak parameters (x_i, w_i, A_i) of the G*, 2D, D+D’ and 2D’ bands. Illustrative examples of the fittings of the first- and second-order Raman spectra of the powders are provided in figures 2c and 2d. The obtained positions and widths of the peaks are presented in the tables S1 and S2 in the supplementary section.

The intensity ratios (by means of integrated areas) of the defect-related bands respect to the G peak are presented in figure 3. The data are also collected as supplementary information in table S3. As expected, high values of A_{D*}/A_G, A_D/A_G and $A_{D'}/A_G$ were obtained for the as-received powders, since GO can be understood as a graphene with many structural and chemical defects. Moreover, the existence of the D+D’ combination mode (~2920 cm^{-1}) with also a high $A_{D+D'}/A_G$ supports the presence of great disorder in the GO structure. When mixing the GO with the zirconia powder, similar A_D/A_G, $A_{D'}/A_G$ and $A_{D+D'}/A_G$ ratios were obtained for both processing methods. This suggests that the GO structure was not altered or damaged during none of the powder processing routines. Figure 3c presents also similar $A_{D''}/A_G$ values in the as-received GO powder and in the composite powders. The D” peak has been reported to be related to the presence of amorphous lattices by Vollebregt et al. [31], so the high obtained ratios

(ranging from 0.40 to 0.76) reveal the presence of these type of defect in the powders. Regarding the D* peak, this band is related to disordered defects provided by the existence of sp^3 bonds in the graphene oxide sheets, and Claramunt et al. reported that this band is intimately related with the oxygen content [24]. The obtained A_{D*}/A_G ratio for the GO powders varies in a large range revealing that the presence of this type of defect is not homogeneous along the GO sheets.

Furthermore, the existence of oxygen bonds and partial amorphization is pointed out by the presence of a broad 2D band with low intensity in both the as-received GO and composite powders [33].

Casallas-Caicedo et al. have recently reported that reduction may occur in GO after long milling times [34]. However, the experimental Raman results in this work are not conclusive in this respect and do not show a significant incipient reduction in the composite powders prepared by PBM compared to the colloidal ones.

After sintering, a remarkable change in the spectra collected from the composites is observed (figure 4a and 4b). A sharpening of the D and G_{app} peaks is clearly observed. The G*, D+D' and 2D' bands look more defined and the 2D band appears as a well-defined band at ~2695 cm^{-1}. Figures 4c and 4d show illustrative examples of the fittings of the first- and second-order Raman spectra carried out using the functions described in §2.2.2. It is worth emphasizing that the best fit for the 2D band was achieved by using three Lorentz peaks. Considering that the line shape of the 2D band is commonly associated with layer stacking [35,36], this fitting of the 2D peak directly suggests that the graphene material present in the composites may include less than 10 layers [37].

The parameters obtained from these fittings –bands position, width and intensity– are presented in the tables S2, S4 and S5 in the supplementary section. These parameters

have been shown to be highly dependent on the presence of defects on the structure of GBN [18,32,38], so the comparison of the obtained values before and after the sintering treatment will elucidate the GO *in-situ* reduction process.

The relative intensities of the defect-related bands (D, D', D" and D+D') respect to the G peak remarkably decrease after sintering (figure 3), indicating that the presence of disorder in the graphene phase of the sintered composites is significantly smaller than in the composite powders and that a partial restoration of the graphene structure has been achieved. Moreover, the remarkable decrease of the $A_{D"}/A_G$ ratio (down to 0.044) after sintering the composites, indicates that the presence of amorphous C phases has also decreased [24,31]. Figure 5a reflects that there is also a noteworthy increase of the A_{2D}/A_G ratio in the sintered composites. This remarkable increase of the intensity of the 2D band has been previously associated with the reduction of GO by Betriu et al. [18]. Thus, all these results suggest that the GO in the composites has been *in-situ* reduced during SPS, becoming reduced graphene oxide (rGO).

The width of the D, G and 2D bands has also been previously pointed out as a suitable parameter to indicate the reduction of GO, as lower peaks widths are observed in rGO in comparison with GO [18]. A decrease of the width of the D and G bands is clearly observed in all the sintered composites (supplementary table S2), however, the fit of the 2D band by using three Lorentz peaks hinders the direct measure of the whole band width. Martins Ferreira et al. [38] have suggested that, in order to consider all the peaks that compose the 2D band in multilayered graphene, it is preferred to analyze the evolution of the width of the band by means of the integrated area divided by the intensity (A_{2D}/I_{2D}), as all the peaks would be represented in the whole area of the band. Figure 5b represents this ratio for the composite powders and the sintered composites,

and a remarkable reduction of the width of the 2D band can be observed after the sintering process. Thus, the analysis of the bands widths supports the conclusion that the GO has been *in-situ* reduced during SPS.

A close analysis of the intensity ratios and band widths for the composites sintered from the powders processed using the two different routines can give an insight into the differences between them in terms of GO reduction. While similar G peak widths have been obtained for all the sintered composites, the width of the D band of the PBM composites is systematically lower than the one of the colloidal composites (supplementary table S2). Moreover, the A_{2D}/I_{2D} values of the composites prepared through the PBM routine (from 130 to 145 cm^{-1}) are lower than the ones obtained for the composites prepared through the colloidal method (from 149 to 161 cm^{-1}). According to Martins Ferreira et al.[38], the variation of the width of the G peak with the number of defects is less pronounced than the variation of the width of the D and 2D bands. Thus, the lower widths of the D and 2D bands in the PBM composites point to a higher reduction level in these composites, in comparison with the composites prepared by the colloidal routine. Furthermore, this conclusion is supported by the higher A_{2D}/A_G –enhanced 2D band sharpening- and lower $A_{D''}/A_G$ of the PBM sintered composites (supplementary table S5) in comparison with the colloidal ones, as these intensity ratios are linked to the graphene restoration and the decrease of the amorphous carbon phases, respectively.

Regarding the bands positions, the D and G peaks frequencies remain approximately constant (supporting tables S1 and S4) when sintering takes places, showing that the C-C are still sp^2 bonds [38]. The position of the D' peak shifts to slightly higher frequencies, which is indicative of the recovering of the hexagonal carbon structure.

Moreover, a shift of the D" peak position to lower frequencies is detected (supplementary table S4), which indicates also a decrease of the oxygen content and the subsequent reduction of the GO during the sintering process [24].

It is worth mentioning that the standard deviation of the previously discussed Raman data is not so high, which indicates the uniformity of the graphene phase throughout the ceramic matrix and that the obtained Raman results are representative of the whole sample.

BSE-SEM has been used to inspect the distribution of the rGO phase in the ceramic matrix (Figure 6). The average atomic number difference between the two phases of the composite allows the identification of a dark phase (rGO) and a light phase (3YTZP). Independently on the rGO content or the powder processing routine used, the BSE-SEM images show a noticeable microstructural anisotropy in the composites. Due to the two-dimensional nature of rGO and the sintering under uniaxial pressure conditions, the nanostructure tends to align with its major surface in the direction perpendicular to the SPS pressing axis. For low rGO content, a remarkable different distribution of the rGO within the zirconia matrix is observed depending on the processing routine used. In the 1rGO_PBM composite, the rGO is quite homogeneously distributed and appears as thinner and shorter layers throughout the entire matrix (figure 6e). By contrast, the 1rGO_C composite exhibits thicker and larger agglomerates (> 30 μm-length) of rGO (figure 6a). A similar distribution is observed for the composite with 2.5 vol% rGO (figure 6b and 6f). In the 2.5rGO_C composite, the rGO agglomerates lead to quite large regions of ceramic phase without rGO, while in the 2.5rGO_PBM composite, several thinner and shorter layers of rGO appear throughout the ceramic matrix. This difference suggests that the synergistic use of the ultrasonic probe and the planetary ball

mill avoids agglomeration of the rGO for low contents. In figures 6c, 6d, 6g and 6h, corresponding to the composites with higher rGO contents (5 and 10 vol%), a network of better interconnected groups of rGO is observed, but no remarkable differences between the two powder processing methods are detected. Due to the lubricating effect of rGO, the PBM effect is minimized for increasing rGO content [20,39].

It is suggested that the observed PBM effect on the size and distribution of the rGO phase could be the cause of the higher level of reduction of GO in these composites compared to that of the colloidal ones. Since the PBM routine produces composites with a better distribution of exfoliated GO layers, there would be more GO surfaces exposed to the reduction process.

Table 1 shows the shape factor and size of the ceramic grains in the sintered composites. Independently of the content of rGO or the powder processing method used, the ceramic grains are equiaxed in all the composites and present a similar shape factor than the one reported for the monolithic 3YTZP prepared in the same SPSed conditions ($F = 0.7 \pm 0.1$) [27]. Previous studies reported that the addition of a GBN filler decreases the grain size of the ceramic matrix and that the refinement effect depends on the thickness and content of the GBNs [40]. In this work, however, no refinement effect on the zirconia grain size has been detected in the composites. The composites prepared using the PBM routine present similar grain size to the monolithic zirconia one (0.29 ± 0.02 μm [27]). On the other hand, the grain size of the composites prepared through the colloidal method are slightly higher. Moreover, the ceramic grain size distribution in those composites are wider than in the ones prepared through the PBM routine, which could be attributed to the lower homogeneity and larger rGO agglomerations observed in the BSE-SEM images of the colloidal samples with low rGO content.

3.2. Elastic modulus and Vickers hardness

The Young's modulus (E), measured by the impulse excitation technique, decreased as the content of rGO increased. This decrease has already been reported to be a consequence of the addition of a more elastic phase to the rigid ceramic matrix [39].

The composite hardness acquired on the top view and cross sections is shown in table 2. The obtained values have been compared to that of a monolithic 3YTZP sintered in the same conditions, which was estimated as 13.9 ± 0.5 GPa in a previous work [41]. Independently of the powder routine used, values similar to the monolithic zirconia were obtained in the composites with 1 vol% rGO. As the content of rGO increased, the hardness of the composites decreased. Previous studies also reported this decrease of hardness with increasing graphene content [14,27]. The hardness of the composites has been commonly related to the ceramic grain size or the residual porosity of the samples. Since the grain size of the composites in this study do not significantly vary and the relative densities of the composites are similar, the decrease in hardness is attributed to the addition of the softer graphene phase into the harder ceramic matrix. It was not feasible to measure the hardness in the composites with 10 vol% rGO, independently of the powder processing routine used, due to lack of well-defined imprints after Vickers indentation on these samples. The same problem was observed on the top view sections of the samples with 5 vol% rGO. For lower rGO contents (1 and 2.5 vol%), no differences between the top view and cross section hardness values were detected. Therefore, despite the anisotropy observed in the BSE-SEM images, no anisotropy has been found in their hardness properties.

3.3. Electrical properties

Graphene oxide is an electrical insulator but when it is reduced, its crystal structure is restored and becomes similar to the one of graphene. Therefore, it is transformed into an electro-conductive material. The GO in the composites was *in-situ* reduced during the sintering process, as confirmed by the Raman analysis, so it is expected that electrical conductivity would be conferred to the ceramic composite if the sufficient amount of rGO is added. It has been reported that reduced zirconia can present some electrical conductivity depending on the reduction level, due to the increase of the oxygen vacancies and presence of injected electrons in the structure. However, the reduction level of 3YTZP sintered at 1250ºC does not introduce enough electrons to allow the electronic conductivity of the ceramic at room temperature [26]. Therefore, the electrical conductivity of the composites in this work is attributed only to the rGO phase.

Due to the anisotropic microstructure of the composite observed by BSE-SEM (figure 6), the composites could behave differently along their two main orientations as it has been previously reported [42–44]. Accordingly, the electrical conductivity of the composites was acquired in two electrode configurations (table 3). The electrical conductivity perpendicular ($\sigma_{\perp}$) to the SPS pressing axis was higher than the parallel one ($\sigma_{\parallel}$) in all the composites. Hence, the composites present an anisotropic electrical behavior independently of the rGO content or the powder processing routine. As the content of rGO increases, the electrical anisotropy decreased and similar $\sigma_{\perp}/\sigma_{\parallel}$ ratios were obtained in the composites with similar rGO content independently of the powder processing routine.

The composites with 1 and 2.5 vol% rGO prepared following the colloidal method are both electrically isolating. An increase up to 5 vol% rGO content drastically increases the electrical conductivity of these composites, situating the percolation threshold between 2.5 and 5 vol% rGO. This percolation value agrees to that observed by other authors who also use rGO as filler in 3YTZP composites [13,14]. When using the PBM routine, however, the percolation threshold is remarkably reduced and the addition of 2.5 vol% rGO leads to an electrically conductive composite. A conductivity of ~ 1.5 S/m in the perpendicular direction is reached, which is significantly higher than the one reported by Shin et al. for a similar rGO content [14] and could allow the EDM of the sample [12]. For 5 vol% rGO composites, the obtained electrical conductivities when they were prepared through the PBM routine are up to four times higher than when they were prepared by the colloidal method. Although no remarkable differences were observed in the BSE-SEM images of these composites (figure 6c and 6g), the obtained difference in their electrical conductivities reveals that the distribution of the rGO in the one prepared by PBM could be better than in the one prepared by the colloidal routine. Moreover, the degree of reduction of the rGO also plays an important role in its electrical response [18], and therefore, in the electrical behavior of the composites. According to the Raman analysis performed in the previous section of this work, the rGO in the samples prepared by the PBM routine present a higher degree of reduction than in the colloidal ones. Thus, the higher electrical conductivity of the 5rGO_PBM composite could be associated also to a better restoration of the graphene structure in these samples. Finally, the highest electrical conductivities were obtained for the composites with 10 vol% rGO, since the rGO content increase enhances the rGO network. Values in the same order of magnitude are found for the composites prepared by the two different routines, in accordance with the lack of microstructural differences

between them. In this case, although the composite prepared by PBM presents a higher degree of reduction of the GO, the electrical conductivity of the 10rGO_C is higher than the 10rGO_PBM. In these two composites, a slight difference of the real %C (and consequently, the GO content) was found by elemental microanalysis, which would explain this anomaly.

4. Conclusions

Nearly fully dense 3YTZP composites with 1, 2.5, 5 and 10 vol% of rGO were consolidated by SPS from powders prepared by two different powder processing routines. The *in-situ* reduction of GO was successfully achieved during sintering, resulting in the presence of rGO with less than 10 layers in the composites, as revealed by the Raman spectroscopy study.

The application of ultrasonication and wet planetary ball milling during the composite powder processing produced a better distribution of the rGO in the ceramic matrix of composites with low rGO content (1 and 2.5 vol%) than when a colloidal technique was used, while no remarkable differences were found in the distribution of larger amounts of rGO (5 and 10 vol%). A remarkable microstructural anisotropy was observed in all the composites, with the rGO aligned with its major surface in the direction perpendicular to the SPS pressing axis. Although this anisotropy was not reflected on the hardness of the composites, a remarkable electrical anisotropy was found in all the composites, with higher conductivities in the direction perpendicular to the pressing axis during sintering.

The better distribution of the rGO throughout the ceramic matrix, together with the higher level of reduction achieved in the composites prepared by the combination of ultrasonication and wet planetary ball milling resulted in a better behavior in terms of

electrical conductivity in these composites: the electrical percolation threshold was reduced below 2.5 vol% of rGO and electrical conductivities higher than 600 S/cm were obtained.

Acknowledgements

This research was supported by the Ministerio de Economía y Competitividad (MINECO) under the project MAT2015-67889-P, cofunded by European funding (ERDF); and by the Ministerio de Ciencia, Innovación y Universidades (MCIU) under the project PGC 2018-101377-B-100 (MCIU/AEI/FEDER, UE). C. López-Pernía acknowledges the financial support of MINECO through the FPI contract ref: BES-2016-078711. F. Gotor and J.M. Córdoba are also gratefully acknowledged for providing access to the planetary ball milling.

References

[1] A. Nieto, A. Bisht, D. Lahiri, C. Zhang, A. Agarwal, Graphene reinforced metal and ceramic matrix composites: a review, Int. Mater. Rev. 62 (2017) 241–302. doi:10.1080/09506608.2016.1219481.

[2] P. Miranzo, M. Belmonte, M.I. Osendi, From bulk to cellular structures: A review on ceramic/graphene filler composites, J. Eur. Ceram. Soc. 37 (2017) 3649–3672. doi:10.1016/j.jeurceramsoc.2017.03.016.

[3] V. Singh, D. Joung, L. Zhai, S. Das, S.I. Khondaker, S. Seal, Graphene based materials: Past, present and future, Prog. Mater. Sci. 56 (2011) 1178–1271. doi:10.1016/j.pmatsci.2011.03.003.

[4] J.R. Potts, D.R. Dreyer, C.W. Bielawski, R.S. Ruoff, Graphene-based polymer nanocomposites, Polymer (Guildf). 52 (2011) 5–25. doi:10.1016/j.polymer.2010.11.042.

[5] S. Gambhir, R. Jalili, D.L. Officer, G.G. Wallace, Chemically converted graphene: scalable chemistries to enable processing and fabrication, NPG Asia Mater. 7 (2015) e186–e186. doi:10.1038/am.2015.47.

[6] L.S. Walker, V.R. Marotto, M.A. Rafiee, N. Koratkar, E.L. Corral, Toughening in Graphene Ceramic Composites, ACS Nano. 5 (2011) 3182–3190. doi:10.1021/nn200319d.

[7] C. Ramírez, S.M. Vega-Diaz, A. Morelos-Gómez, F.M. Figueiredo, M. Terrones, M.I. Osendi, M. Belmonte, P. Miranzo, Synthesis of conducting graphene/Si3N4 composites by spark plasma sintering, Carbon N. Y. 57 (2013) 425–432.

doi:10.1016/j.carbon.2013.02.015.

[8] C. Ramirez, P. Miranzo, M. Belmonte, M.I. Osendi, P. Poza, S.M. Vega-Diaz, M. Terrones, Extraordinary toughening enhancement and flexural strength in Si3N4 composites using graphene sheets, J. Eur. Ceram. Soc. 34 (2014) 161–169. doi:10.1016/j.jeurceramsoc.2013.08.039.

[9] O. Hanzel, R. Sedlák, J. Sedláček, V. Bizovská, R. Bystrický, V. Girman, A. Kovalčíková, J. Dusza, P. Šajgalík, Anisotropy of functional properties of SiC composites with GNPs, GO and in-situ formed graphene, J. Eur. Ceram. Soc. 37 (2017) 3731–3739. doi:10.1016/j.jeurceramsoc.2017.03.060.

[10] K. Wang, Y. Wang, Z. Fan, J. Yan, T. Wei, Preparation of graphene nanosheet/alumina composites by spark plasma sintering, Mater. Res. Bull. 46 (2011) 315–318. doi:10.1016/j.materresbull.2010.11.005.

[11] Q. Wang, Y. Li, M. Luo, S. Sang, T. Zhu, L. Zhao, Strengthening mechanism of graphene oxide nanosheets for Al2O3–C refractories, Ceram. Int. 40 (2014) 163–172. doi:10.1016/j.ceramint.2013.05.117.

[12] A. Centeno, V.G. Rocha, B. Alonso, A. Fernández, C.F. Gutierrez-Gonzalez, R. Torrecillas, A. Zurutuza, Graphene for tough and electroconductive alumina ceramics, J. Eur. Ceram. Soc. 33 (2013) 3201–3210. doi:10.1016/j.jeurceramsoc.2013.07.007.

[13] N.W. Solís, P. Peretyagin, R. Torrecillas, A. Fernández, J.L. Menéndez, C. Mallada, L.A. Díaz, J.S. Moya, Electrically conductor black zirconia ceramic by SPS using graphene oxide, J. Electroceramics. 38 (2017) 119–124. doi:10.1007/s10832-017-0076-z.

[14] J.-H. Shin, S.-H. Hong, Fabrication and properties of reduced graphene oxide reinforced yttria-stabilized zirconia composite ceramics, J. Eur. Ceram. Soc. 34 (2014) 1297–1302. doi:10.1016/j.jeurceramsoc.2013.11.034.

[15] W. Gao, The chemistry of graphene oxide, Graphene Oxide Reduct. Recipes, Spectrosc. Appl. (2015) 61–95. doi:10.1007/978-3-319-15500-5_3.

[16] Z. Zeng, Y. Liu, W. Chen, X. Li, Q. Zheng, K. Li, R. Guo, Fabrication and properties of in situ reduced graphene oxide-toughened zirconia composite ceramics, J. Am. Ceram. Soc. 101 (2018) 3498–3507. doi:10.1111/jace.15483.

[17] H. Xia, X. Zhang, Z. Shi, C. Zhao, Y. Li, J. Wang, G. Qiao, Mechanical and thermal properties of reduced graphene oxide reinforced aluminum nitride ceramic composites, Mater. Sci. Eng. A. 639 (2015) 29–36. doi:10.1016/j.msea.2015.04.091.

[18] X. Díez-Betriu, S. Álvarez-García, C. Botas, P. Álvarez, J. Sánchez-Marcos, C. Prieto, R. Menéndez, A. De Andrés, Raman spectroscopy for the study of reduction mechanisms and optimization of conductivity in graphene oxide thin films, J. Mater. Chem. C. 1 (2013) 6905–6912. doi:10.1039/c3tc31124d.

[19] R.C. Garvie, R.H. Hannink, R.T. Pascoe, Ceramic steel?, Nature. 258 (1975) 703–704. doi:10.1038/258703a0.

[20] M. Michálková, M. Kašiarová, P. Tatarko, J. Dusza, P. Šajgalík, Effect of homogenization treatment on the fracture behaviour of silicon nitride/graphene nanoplatelets composites, J. Eur. Ceram. Soc. 34 (2014) 3291–3299. doi:10.1016/j.jeurceramsoc.2014.03.023.

[21] C. López-Pernía, C. Muñoz-Ferreiro, C. González-Orellana, A. Morales-Rodríguez, Á. Gallardo-López, R. Poyato, Optimizing the homogenization technique for graphene nanoplatelet/yttria tetragonal zirconia composites: Influence on the microstructure and the electrical conductivity, J. Alloys Compd. 767 (2018) 994–1002. doi:10.1016/j.jallcom.2018.07.199.

[22] M. Boniecki, P. Gołębiewski, W. Wesołowski, M. Woluntarski, A. Piątkowska, M. Romaniec, P. Ciepielewski, K. Krzyżak, Alumina/zirconia composites toughened by the addition of graphene flakes, Ceram. Int. 43 (2017) 10066–10070. doi:10.1016/j.ceramint.2017.05.025.

[23] F. Chen, D. Jin, K. Tyeb, B. Wang, Y.H. Han, S. Kim, J.M. Schoenung, Q. Shen, L. Zhang, Field assisted sintering of graphene reinforced zirconia ceramics, Ceram. Int. 41 (2015) 6113–6116. doi:10.1016/j.ceramint.2014.12.147.

[24] S. Claramunt, A. Varea, D. López-Díaz, M.M. Velázquez, A. Cornet, A. Cirera, The importance of interbands on the interpretation of the raman spectrum of graphene oxide, J. Phys. Chem. C. 119 (2015) 10123–10129. doi:10.1021/acs.jpcc.5b01590.

[25] A. Sadezky, H. Muckenhuber, H. Grothe, R. Niessner, U. Pöschl, Raman microspectroscopy of soot and related carbonaceous materials: Spectral analysis and structural information, Carbon N. Y. 43 (2005) 1731–1742. doi:10.1016/j.carbon.2005.02.018.

[26] R. Poyato, J. Macías-Delgado, A. García-Valenzuela, R.L. González-Romero, A. Muñoz, A. Domínguez-Rodríguez, Electrical properties of reduced 3YTZP ceramics consolidated by spark plasma sintering, Ceram. Int. 42 (2016) 6713–

6719. doi:10.1016/j.ceramint.2016.01.040.

[27] A. Gallardo-López, I. Márquez-Abril, A. Morales-Rodríguez, A. Muñoz, R. Poyato, Dense graphene nanoplatelet/yttria tetragonal zirconia composites: Processing, hardness and electrical conductivity, Ceram. Int. 43 (2017) 11743–11752. doi:10.1016/j.ceramint.2017.06.007.

[28] C. Muñoz-Ferreiro, A. Morales-Rodríguez, T.C. Rojas, E. Jiménez-Piqué, C. López-Pernía, R. Poyato, A. Gallardo-López, Microstructure, interfaces and properties of 3YTZP ceramic composites with 10 and 20 vol% different graphene-based nanostructures as fillers, J. Alloys Compd. 777 (2019) 213–224. doi:10.1016/j.jallcom.2018.10.336.

[29] L.M. Malard, M.A. Pimenta, G. Dresselhaus, M.S. Dresselhaus, Raman spectroscopy in graphene, Phys. Rep. 473 (2009) 51–87. doi:10.1016/j.physrep.2009.02.003.

[30] R. Rozada, J.I. Paredes, S. Villar-Rodil, A. Martínez-Alonso, J.M.D. Tascón, Towards full repair of defects in reduced graphene oxide films by two-step graphitization, Nano Res. 6 (2013) 216–233. doi:10.1007/s12274-013-0298-6.

[31] S. Vollebregt, R. Ishihara, F.D. Tichelaar, Y. Hou, C.I.M. Beenakker, Influence of the growth temperature on the first and second-order Raman band ratios and widths of carbon nanotubes and fibers, Carbon N. Y. 50 (2012) 3542–3554. doi:10.1016/j.carbon.2012.03.026.

[32] D. López-Díaz, M. López Holgado, J.L. García-Fierro, M.M. Velázquez, Evolution of the Raman Spectrum with the Chemical Composition of Graphene Oxide, J. Phys. Chem. C. 121 (2017) 20489–20497.

doi:10.1021/acs.jpcc.7b06236.

[33] A. Ganguly, S. Sharma, P. Papakonstantinou, J. Hamilton, Probing the thermal deoxygenation of graphene oxide using high-resolution in situ X-ray-based spectroscopies, J. Phys. Chem. C. 115 (2011) 17009–17019. doi:10.1021/jp203741y.

[34] F.M. Casallas Caicedo, E. Vera López, A. Agarwal, V. Drozd, A. Durygin, A. Franco Hernandez, C. Wang, Synthesis of graphene oxide from graphite by ball milling, Diam. Relat. Mater. 109 (2020) 108064. doi:10.1016/j.diamond.2020.108064.

[35] A.C. Ferrari, J.C. Meyer, V. Scardaci, C. Casiraghi, M. Lazzeri, F. Mauri, S. Piscanec, D. Jiang, K.S. Novoselov, S. Roth, A.K. Geim, Raman spectrum of graphene and graphene layers, Phys. Rev. Lett. 97 (2006).

[36] L.M. Malard, M. a. Pimenta, G. Dresselhaus, M.S. Dresselhaus, Raman spectroscopy in graphene, Phys. Rep. 473 (2009) 51–87. doi:10.1016/j.physrep.2009.02.003.

[37] M. Sahoo, R.P. Antony, T. Mathews, S. Dash, A.K. Tyagi, Raman studies of chemically and thermally reduced graphene oxide, in: AIP Conf. Proc. 1512, 2013: pp. 1262–1263. doi:10.1063/1.4791511.

[38] E.H. Martins Ferreira, M.V.O. Moutinho, F. Stavale, M.M. Lucchese, R.B. Capaz, C.A. Achete, A. Jorio, Evolution of the Raman spectra from single-, few-, and many-layer graphene with increasing disorder, Phys. Rev. B - Condens. Matter Mater. Phys. 82 (2010). doi:10.1103/PhysRevB.82.125429.

[39] Á. Gallardo-López, J. Castillo-Seoane, C. Muñoz-Ferreiro, C. López-Pernía, A. Morales-Rodríguez, R. Poyato, Flexure Strength and Fracture Propagation in Zirconia Ceramic Composites with Exfoliated Graphene Nanoplatelets, Ceramics. 3 (2020) 78–91. doi:10.3390/ceramics3010009.

[40] Á. Gallardo-López, C. López-Pernía, C. Muñoz-Ferreiro, C. González-Orellana, A. Morales-Rodríguez, R. Poyato, Spark Plasma Sintered Zirconia Ceramic Composites with Graphene-Based Nanostructures, Ceramics. 1 (2018) 153–164. doi:10.3390/ceramics1010014.

[41] C. Muñoz-Ferreiro, A. Morales-Rodríguez, T.C. Rojas, E. Jiménez-Piqué, C. López-Pernía, R. Poyato, A. Gallardo-López, Microstructure, interfaces and properties of 3YTZP ceramic composites with 10 and 20 vol% different graphene-based nanostructures as fillers, J. Alloys Compd. 777 (2019) 213–224. doi:10.1016/j.jallcom.2018.10.336.

[42] O. Tapasztó, L. Tapasztó, H. Lemmel, V. Puchy, J. Dusza, C. Balázsi, K. Balázsi, High orientation degree of graphene nanoplatelets in silicon nitride composites prepared by spark plasma sintering, Ceram. Int. 42 (2016) 1002–1006. doi:10.1016/j.ceramint.2015.09.009.

[43] C. Ramirez, L. Garzón, P. Miranzo, M.I. Osendi, C. Ocal, Electrical conductivity maps in graphene nanoplatelet/silicon nitride composites using conducting scanning force microscopy, Carbon N. Y. 49 (2011) 3873–3880. doi:10.1016/j.carbon.2011.05.025.

[44] R. Poyato, J. Osuna, A. Morales-Rodríguez, Á. Gallardo-López, Electrical conduction mechanisms in graphene nanoplatelet/yttria tetragonal zirconia

composites, Ceram. Int. 44 (2018) 14610–14616. doi:10.1016/j.ceramint.2018.05.082.

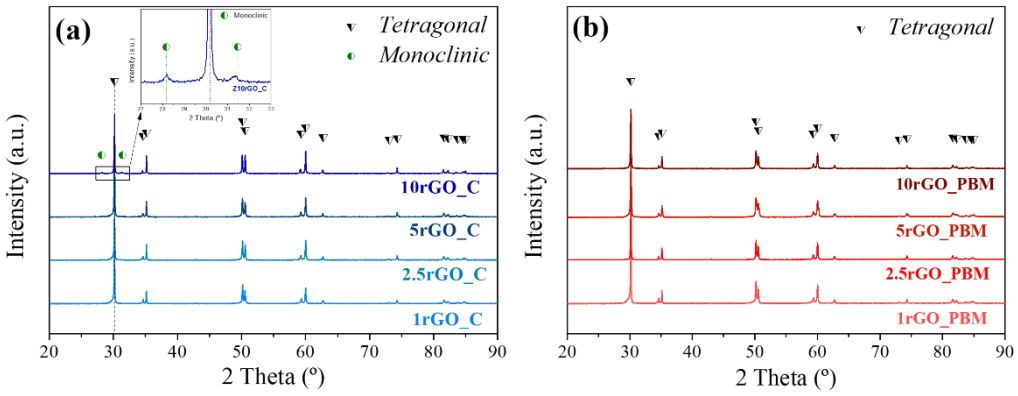

Figure 1. X-ray diffraction patterns of the rGO/3YTZP composites sintered from the powders prepared by (a) the colloidal method and (b) the PBM routine.

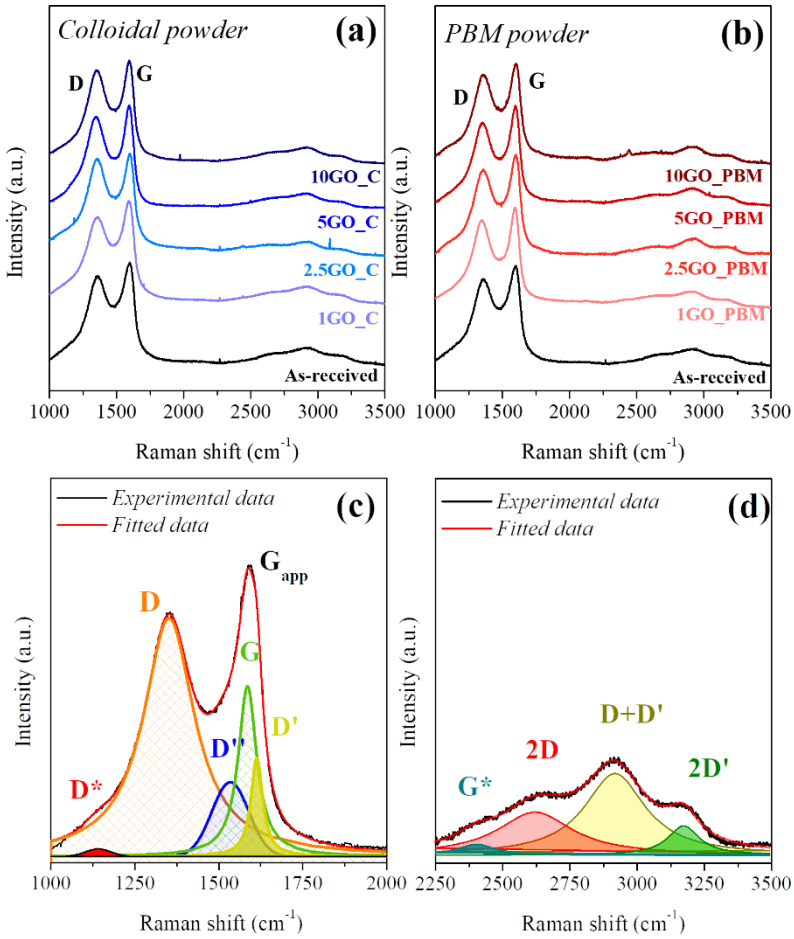

Figure 2. Representative Raman spectra acquired on the as-received GO powders and the composite powders with different content of GO prepared through the (a) colloidal and (b) PBM routines; (c) Illustrative example of the deconvolution of the first-order Raman spectra; (d) Illustrative example of the deconvolution of the second-order Raman spectra.

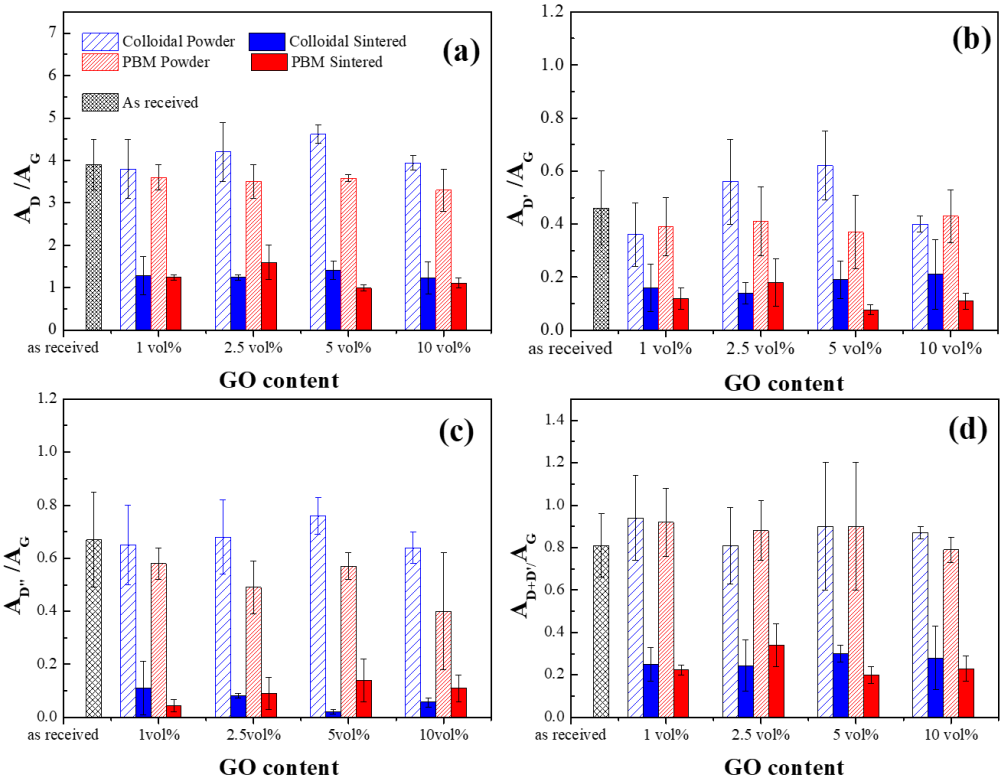

Figure 3. Intensity ratios of the defect related bands with respect to the G peak, obtained for the as-received GO, composites powders and sintered composites; (a) Intensity ratio of the D band; (b) Intensity ratio of the D' band; (c) Intensity ratio of the D" band; (b) Intensity ratio of the D+D'.

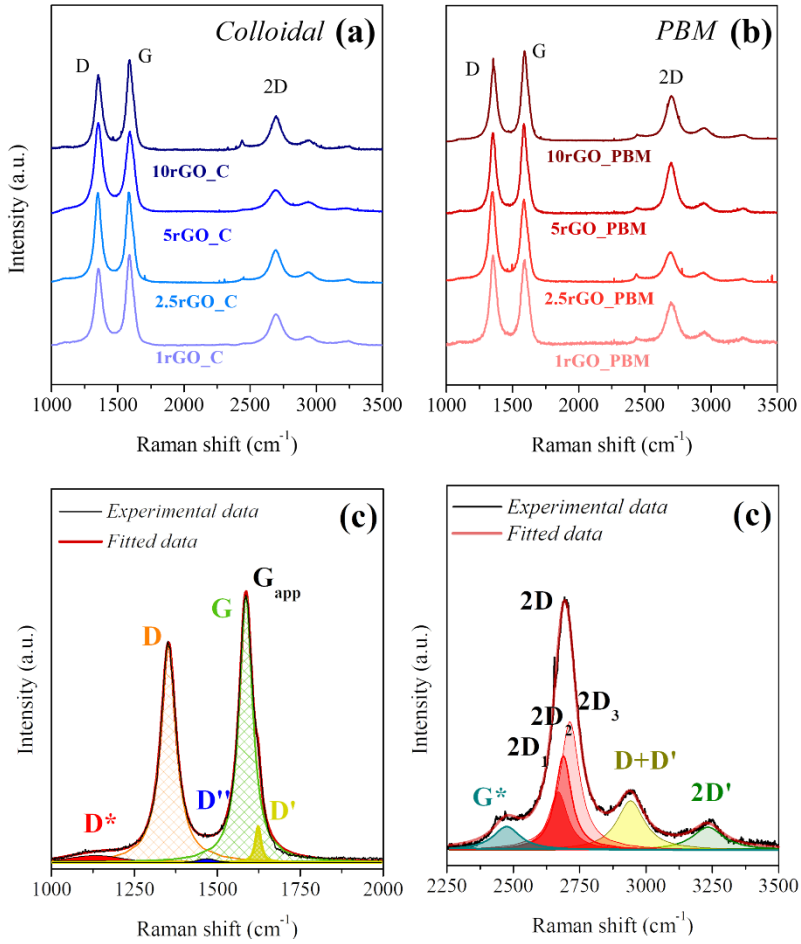

Figure 4. Representative Raman spectra acquired on the sintered composites with different content of rGO prepared through the (a) colloidal and (b) PBM routines; (c) Illustrative example of the deconvolution of the first-order Raman spectra; (d) Illustrative example of the deconvolution of the second-order Raman spectra.

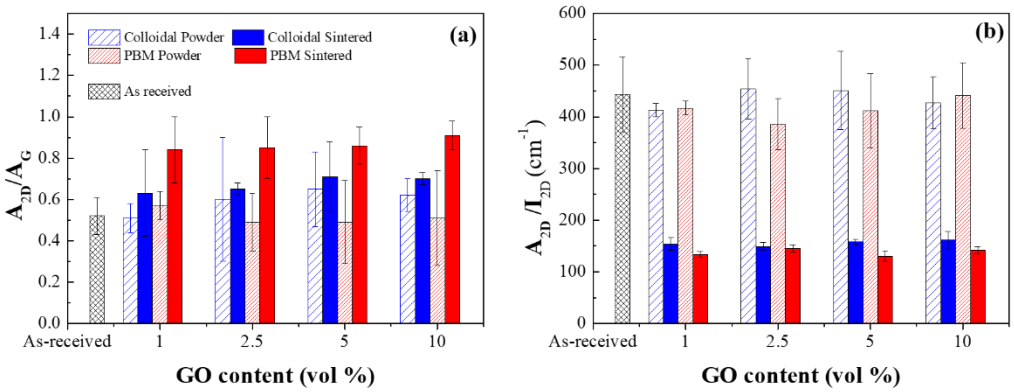

Figure 5. Intensity and width of the 2D band, obtained for the as-received GO, composite powders and sintered composites; (a) Intensity ratio of the 2D band with respect to the G peak; (b) 2D peak width obtained by means of the ratio between the integrated area of the 2D band and the height of the peak.

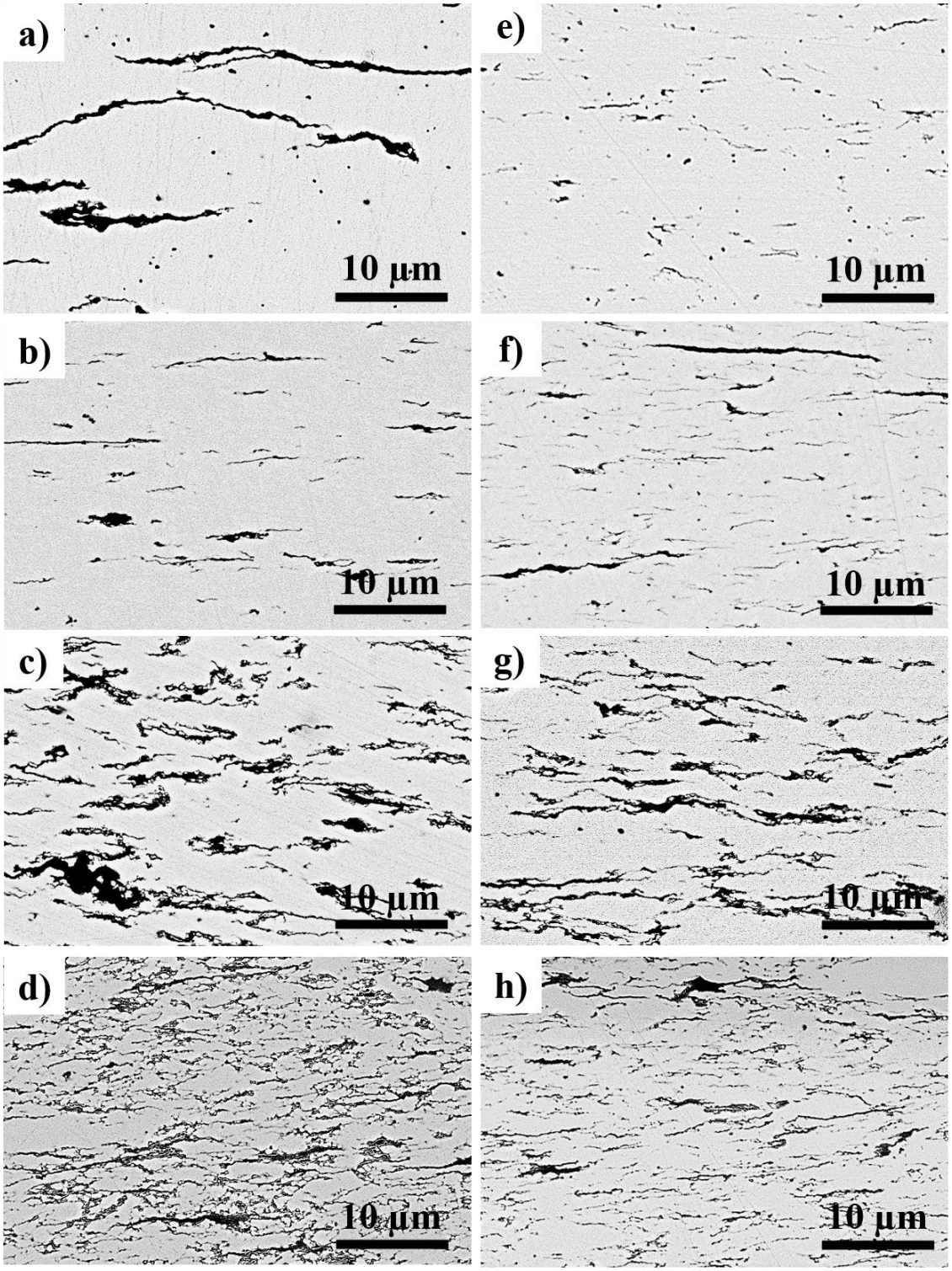

Figure 6. BSE-SEM images from the cross sections of the sintered composites prepared by the colloidal method: (a) 1rGO_C, (b) 2.5rGO_C, (c) 5rGO_C and (d) 10rGO_C rGO; and by the PBM routine: (e) 1rGO_PBM, (f) 2.5rGO_PBM, (g) 5rGO_PBM and (h) 10rGO_PBM.

Table 1. Relative and measured densities of the rGO/3YTZP composites, and mean grain size and shape factor (with their standard deviations) of their ceramic matrices.

Sample	ρ_{rel} (%)	ρ (g/cm^3)	d ± s.d (μm)	F ± s.d.
1rGO_C	100.08 ± 0.06	6.016 ± 0.004	0.26 ± 0.15	0.71 ± 0.09
2.5rGO_C	100.15 ± 0.17	5.963 ± 0.010	0.31 ± 0.17	0.72 ± 0.08
5rGO_C	98.7 ± 0.9	5.78 ± 0.05	0.28 ± 0.16	0.72 ± 0.08
10rGO_C	100.85 ± 0.19	5.713 ± 0.011	0.35 ± 0.23	0.69 ± 0.09
1rGO_PBM	99.59 ± 0.11	5.987 ± 0.006	0.27 ± 0.14	0.71 ± 0.08
2.5rGO_PBM	98.70 ± 0.06	5.876 ± 0.004	0.26 ± 0.14	0.72 ± 0.08
5rGO_PBM	98.41 ± 0.07	5.764 ± 0.004	0.28 ± 0.16	0.71 ± 0.09
10rGO_PBM	99.46 ± 0.15	5.635 ± 0.008	0.27 ± 0.13	0.71 ± 0.09

Table 2. Measured elastic moduli and hardness values of the rGO/3YTZP sintered composites.

Sample	E (GPa)	H_v c.s. (GPa)	H_v t.v. (GPa)
1rGO_C	191 ± 12	13.8 ± 1.2	13.6 ± 0.6
2.5rGO_C	205 ± 14	12.5 ± 1.6	12.5 ± 2.2
5rGO_C	180 ± 13	9.2 ± 0.8	-**
10rGO_C	119.8 ± 1.7	-**	-**
1rGO_PBM	205 ± 7	13.6 ± 0.6	14.2 ± 0.9
2.5rGO_PBM	193 ± 13	11.5 ± 0.5	10.4 ± 0.6
5rGO_PBM	172 ± 12	10.0 ± 0.6	-**
10rGO_PBM	143.9 ± 1.9	-**	-**

**Spalling

Table 3. Measured electrical conductivity and anisotropy factor of the rGO/3YTZP composites.

Sample	$\sigma_{\perp}$ (S/m)	$\sigma_{\parallel}$ (S/m)	$\sigma_{\perp}/\sigma_{\parallel}$
1rGO_C	Not conductive	Not conductive	-
2.5rGO_C	Not conductive	Not conductive	-
5rGO_C	95 ± 5	4.73 ± 0.24	20.1 ± 2.1
10rGO_C	860 ± 120	87 ± 4	9.9 ± 1.8
1rGO_PBM	Not conductive	Not conductive	-
2.5rGO_PBM	1.50 ± 0.08	0.0380 ± 0.0019	40 ± 5
5rGO_PBM	390 ± 20	20.2 ± 1.0	19.4 ± 1.9
10rGO_PBM	610 ± 90	47.8 ± 2.4	13 ± 3

SUPPLEMENTARY INFORMATION

Enhancing the electrical conductivity of in-situ reduced graphene oxide-zirconia composites through the control of the processing routine

Supporting table S1. Positions of the D*, D, D", G, D' and 2D bands obtained for the as-received GO and the composite powders.

Sample	D*(cm^{-1})	D (cm^{-1})	D" (cm^{-1})	G (cm^{-1})	D' (cm^{-1})	2D(cm^{-1})
as-received GO	1150 ± 40	1360 ± 40	1535 ± 11	1588 ± 3	1615 ± 4	2657 ± 11
1GO_C	1140 ± 40	1354.7 ± 0.8	1540 ± 4	1587 ± 4	1616 ± 3	2649 ± 18
2.5GO_C	1143 ± 24	1355 ± 3	1539 ± 4	1587.8 ± 1.5	1614.7 ± 1.0	2629 ± 14
5GO_C	1179 ± 18	1350 ± 4	1539 ± 3	1587 ± 3	1614 ± 3	2661 ± 8
10GO_C	1154 ± 7	1352.2 ±0.8	1538.44 ± 0.21	1587.2 ± 0.5	1614.2 ± 0.5	2657 ± 7
1GO_PBM	1158 ± 23	1350 ± 4	1533.9 ± 0.9	1586.1 ± 0.9	1612.8 ± 1.9	2634 ± 4
2.5GO_PBM	1120 ± 9	1355 ± 4	1534 ± 8	1589 ± 4	1616 ± 3	2616 ± 18
5GO_PBM	1150 ± 40	1349 ± 6	1534 ± 9	1586 ± 2	1612 ± 4	2621 ± 22
10GO_PBM	1118 ± 6	1356 ± 4	1526 ± 4	1587 ± 3	1614 ± 4	2595 ± 16

Supporting table S2. Widths of the D, G and 2D bands obtained for the composite powders and sintered samples

Sample (powder)	D (cm^{-1})	G (cm^{-1})	A_{2D}/I_{2D} (cm^{-1})	**Sample (sintered)**	D (cm^{-1})	G (cm^{-1})	A_{2D}/I_{2D} (cm^{-1})
as-received GO	186 ±15	73 ± 13	440 ± 80	-	-	-	-
1GO_C	196 ± 20	70 ± 8	413 ± 13	1rGO_C	63 ± 5	52 ± 5	154 ± 12
2.5GO_C	182 ± 5	70 ± 7	450± 60	2.5rGO_C	61.8 ± 1.1	52.5 ± 1.6	149 ± 8
5GO_C	176 ± 8	58 ± 7	450 ± 80	5rGO_C	66 ± 7	55 ± 6	158 ± 5
10GO_C	183.47 ± 0.15	66.3 ± 1.0	430 ± 50	10rGO_C	68 ± 8	51 ± 4	161 ± 17
1GO_PBM	184 ± 8	66 ± 3	417 ± 14	1rGO_PBM	59 ± 5	54 ± 4	133 ± 6
2.5GO_PBM	189 ± 9	73 ± 5	390 ± 50	2.5rGO_PBM	61 ± 5	54 ± 4	145 ± 7
5GO_PBM	186 ± 12	70 ± 12	410 ± 70	5rGO_PBM	55.3 ± 1.4	50 ± 3	130 ± 10
10GO_PBM	187 ± 5	80 ± 9	440 ± 60	10rGO_PBM	60 ± 3	52 ± 4	141 ± 7

Supporting table S3. Intensity ratios of the D*, D, D", D', 2D and D+D' bands with respect to the G peak, obtained for the as-received GO powder and the composites powders prepared by the two processing routines.

Sample	A_{D^*}/A_G	A_D/A_G	$A_{D"}/A_G$	$A_{D'}/A_G$	A_{2D}/A_G	$A_{D+D'}/A_G$
as-received GO	0.15 ± 0.08	3.9 ± 0.6	0.67 ± 0.18	0.46 ± 0.14	0.52 ± 0.09	0.81 ± 0.15
1GO_C	0.047 ± 0.010	3.8 ± 0.7	0.65 ±0.15	0.36 ± 0.12	0.51 ± 0.07	0.94 ± 0.02
2.5GO_C	0.064 ± 0.024	4.3 ± 0.7	0.70 ± 0.14	0.56 ± 0.16	0.6 ± 0.3	0.81 ± 0.18
5GO_C	0.13 ± 0.04	4.62 ± 0.21	0.76 ± 0.07	0.62 ± 0.13	0.65 ± 0.18	0.9 ± 0.3
10GO_C	0.055 ± 0.013	3.94 ± 0.17	0.64 ± 0.06	0.40 ± 0.03	0.62 ± 0.08	0.87 ± 0.03
1GO_PBM	0.09 ± 0.05	3.6 ± 0.3	0.58 ± 0.06	0.39 ± 0.11	0.57 ± 0.07	0.92 ± 0.16
2.5GO_PBM	0.07 ± 0.05	3.5 ± 0.5	0.49 ± 0.15	0.41 ± 0.13	0.49 ± 0.14	0.88 ± 0.14
5GO_PBM	0.11 ± 0.08	3.5 ± 0.7	0.56 ± 0.21	0.37 ± 0.14	0.49 ± 0.20	0.9 ± 0.3
10GO_PBM	0.06 ± 0.03	3.3 ± 0.5	0.43 ± 0.22	0.43 ± 0.10	0.51 ± 0.23	0.79 ± 0.06

Supporting table S4. Positions of the D*, D, D", G, D' and 2D bands obtained for the sintered composites

Sample	D*(cm^{-1})	D (cm^{-1})	D" (cm^{-1})	G (cm^{-1})	D'(cm^{-1})	2D(cm^{-1})
1rGO_C	1150 ± 30	1355 ± 3	1490 ± 30	1589 ± 4	1622 ± 6	2696 ± 8
2.5rGO_C	1128 ± 3	1351.2 ± 1.3	1490 ± 6	1585.2 ± 0.8	1619.1 ± 0.9	2693.4 ± 2.3
5rGO_C	1134 ± 23	1354.0 ± 1.9	1487 ± 40	1588.1 ± 1.7	1620.5 ± 2.2	2697 ± 3
10rGO_C	1120 ± 30	1352 ± 3	1490 ± 30	1584.9 ± 1.0	1616.6 ± 1.7	2690 ± 3
1rGO_PBM	1110 ± 13	1354.0 ± 1.0	1459 ± 20	1588.1 ± 1.9	1622.1 ± 2.0	2700.3 ± 2.1
2.5rGO_PBM	1133 ± 25	1349 ± 3	1515 ± 23	1586 ± 2	1619 ± 3	2694 ± 3
5rGO_PBM	1130 ± 5	1353.2 ± 0.6	1464 ± 7	1586.5 ± 0.9	1622.7 ± 1.1	2696.1 ± 1.6
10rGO_PBM	1131.2 ± 1.8	1353 ± 1.1	1501 ± 26	1587.2 ± 1.2	1622.1 ± 0.8	2697 ± 6

Supporting table S5. Intensity ratios of the D*, D, D", D', 2D and D+D' bands with respect to the G peak, obtained for the sintered composites.

Sample	A_{D^*}/A_G	A_D/A_G	$A_{D"}/A_G$	$A_{D'}/A_G$	A_{2D}/A_G	$A_{D+D'}/A_G$
1rGO_C	0.10 ± 0.08	1.3 ± 0.5	0.11 ± 0.10	0.16 ± 0.19	0.63 ± 0.21	0.25 ± 0.08
2.5rGO_C	0.095 ± 0.008	1.23 ± 0.06	0.082 ± 0.008	0.14 ± 0.04	0.65 ± 0.03	0.224 ± 0.012
5rGO_C	0.08 ± 0.03	1.41 ± 0.21	0.14 ± 0.08	0.19 ± 0.07	0.71 ± 0.17	0.30 ± 0.04
10rGO_C	0.08 ± 0.05	1.2 ± 0.4	0.11 ± 0.05	0.21 ± 0.13	0.7 ± 0.3	0.28 ± 0.15
1rGO_PBM	0.059 ± 0.018	1.14 ± 0.15	0.044 ± 0.023	0.12 ± 0.04	0.84 ± 0.16	0.223 ± 0.022
2.5rGO_PBM	0.09 ± 0.05	1.6 ± 0.4	0.09 ± 0.06	0.18 ± 0.09	0.85 ± 0.15	0.34 ± 0.10
5rGO_PBM	0.06 ± 0.03	0.98 ± 0.06	0.019 ± 0.008	0.077 ± 0.019	0.86 ± 0.09	0.20 ± 0.04
10rGO_PBM	0.07 ± 0.03	1.11 ± 0.12	0.049 ± 0.017	0.11 ± 0.03	0.91 ± 0.07	0.26 ± 0.03